

Trends in Biothermophotonics and Bioacoustophotonics of Tissues

A. Mandelis*, R. J. Jeon, S. Telenkov, Y. Fan and A. Matvienko

Center for Advanced Diffusion-Wave Technologies (CADIFT), Dept. of Mechanical and Industrial Engineering, Univ. of Toronto, 5 King's College Road, Toronto, Ontario, M5S 3G8, Canada

ABSTRACT

Recent trends in bioacoustophotonics and biothermophotonics of tissues are presented. The presentation is centered on the development of well-known frequency-domain photothermal and photoacoustic techniques to address issues associated with diffuse photon density waves during optical excitation of turbid media, both in hard tissues (teeth) and soft tissues. These methods have concrete advantages over the conventional pulsed-laser counterparts. In Part I we present biothermophotonic principles and applications to the detection of the carious state in human teeth as embodied by laser photothermal radiometry supported by modulated luminescence. The emphasis is on the abilities of these techniques to approach important problems such as the diagnosis of occlusal pits and fissures and interproximal lesions between teeth which normally go undetected by x-ray radiographs. In Part II we present theoretical and experimental results in frequency-domain bioacoustophotonics of turbid media, such as soft tissues, and we describe the development of sensitive sub-surface imaging methodologies which hold the promise for sensitive diagnostics of cancerous lesions in e.g. a human breast. Results using tissue phantoms and ex-vivo specimens are discussed and the current level of sub-surface lesion sensitivity compared to state-of-the-art pulsed photoacoustic techniques is examined. In summary, advances in coupled frequency-domain diffuse-photon-density-wave and thermal or thermoelastic responses of turbid media constitute new trends in bioacoustophotonics and biothermophotonics promising for their signal quality and high dynamic range.

Keywords: Dental, bioacoustophotonics, biothermophotonics, hard tissue, soft tissue, photothermal radiometry, dental caries detection, depth profilometry, photothermoacoustics, frequency domain, coherence, imaging

1. INTRODUCTION

The fields of biothermophotonics and bioacoustophotonics are the direct evolution of a rich arsenal of photothermal and photoacoustic techniques which have been under development for the past quarter century. The terms "biothermophotonics" and "bioacoustophotonics" are themselves an evolution of conventional photothermal and photoacoustic phenomena with the added complexity of optical propagation in turbid (scattering) tissue in which the heat- and/or sound-generating optical field is the result of diffuse photon density wave propagation in the medium¹. From this perspective, these terms indicate the coupled diffuse-photon-density wave and thermal-wave phenomena in such media, sometimes followed by thermal-to-acoustical energy conversion and detection. Trends in improved diagnostic capabilities, coupled with significantly higher optical damage thresholds for tissue, point toward the use of frequency-domain techniques as the next-generation technologies to supplement or replace pulsed laser photothermal or photoacoustic detection with due attention to the physics of the photon propagation in the scattering medium. Two major areas of development will be discussed in some detail, covering both hard and soft tissue diagnostics. In Part I the use of laser biothermophotonics for dental diagnostics is considered as a promising technique, complementary to the phenomenon of laser-induced fluorescence of enamel or to the fluorescence caused by porphyrins present in carious tissue^{2,3}. The first attempt to apply the depth profilometric capability of frequency-domain laser infrared photothermal radiometry (PTR) toward the inspection of dental defects was reported by Mandelis *et al.*⁴ and Nicolaidis *et al.*⁵ and was reviewed by Mandelis⁶. An evaluation of this technology to occlusal pit and fissure and interproximal lesion detection will be discussed. In Part II of this paper, the field of laser bioacoustophotonics is introduced within the context of photothermoacoustic (PTA) frequency-domain techniques and their applications to imaging of soft tissues. The coupling of diffuse-photon-density-wave and thermal-wave problems is an important issue toward the full development of the diagnostic opportunities of this area. The PTA approach to non-invasive imaging of biomaterials takes advantage of high optical contrast of tissue chromophores and the ability of acoustic waves to travel long

* mandelis@mie.utoronto.ca; phone/fax 1 416 978-5106; cadift.mie.utoronto.ca

distances without significant distortion or attenuation. The general field of biomedical optoacoustics has so far been based entirely on pulsed laser excitation and time-of-flight measurements of acoustic transients to determine spatial position and optical properties of subsurface chromophores (blood vessels, tumors, tissue pigments and analytes⁷⁻⁹). The field has experienced very rapid development in recent years¹⁰⁻¹² due to promising results demonstrated in PTA experiments for profilometric measurements and imaging of turbid media at depths significantly larger than accessible by purely optical methodologies^{7,13}. Although pulsed methods provide a number of advantages, there are certain difficulties for imaging applications and clinical implementation of the pulsed PTA technique. First, time-resolved measurements require wide-band (1 – 100 MHz) ultrasonic transducers and the signal-to-noise ratio (SNR) must be sufficiently high for wide detection bandwidths. Second, the inherently bipolar shape of acoustic transients and laser jitter noise make precise measurements of subsurface chromophore position difficult. Third, the high peak power of laser pulses needed to deliver optical excitation to deep tissue layers may cause an adverse reaction in live human tissue. To overcome these difficulties of the pulsed PTA technique, a novel frequency domain photoacoustic (FD-PTA) imaging methodology will be described, featuring linear frequency modulated (LFM) optical excitation and coherent detection of the photoacoustic response to determine the spatial position and optical parameters of sub-surface tissue chromophores. The main features of the FD-PTA technique are: a) the acoustic wave is generated by periodic modulation of a near-IR CW laser using LFM waveforms; b) depth information on sub-surface tissue structures is derived from the spectrum of the PTA signals; c) coherent signal processing is utilized to improve SNR; d) time-domain PTA response is reconstructed from frequency scans using inverse Fourier transforms. The FD-PTA system can be used for both single-point depth profilometry and two-dimensional slice imaging of turbid media with optical absorption contrast at the wavelength of laser irradiation.

2. BIOTHERMOPHOTONICS OF HARD TISSUES: APPLICATIONS TO DENTAL CARIES

Nowadays with the widespread use of fluoride, the prevalence of caries, particularly smooth surface caries has been considerably reduced¹⁴, but the development of a non-invasive, non-contacting technique which can detect early demineralization on or beneath the enamel surface is essential for the clinical management of this problem. A novel biothermophotonic technique has been introduced, based on the modulated thermal infrared (black-body or Planck radiation) response of a turbid medium, resulting from radiation absorption and non-radiative energy conversion followed by a small temperature rise. Thus, PTR has the ability to penetrate, and yield information about, an opaque medium well beyond the range of optical imaging. Specifically, the frequency dependence of the penetration depth of thermal waves makes it possible to perform depth profiling of materials¹⁵. In PTR applications to turbid media, such as hard dental tissue, depth information is obtained following optical-to-thermal energy conversion and transport of the incident laser power in two distinct modes: conductively, from a near-surface distance (50 ~ 500 μ m) controlled by the thermal diffusivity of enamel; and radiatively, through blackbody emissions from considerably deeper regions commensurate with the optical penetration of the diffusely scattered laser-induced optical field (several mm)^{15,16}.

2.1. Depth-profilometric characterization of human teeth

2.1.1. Experimental apparatus

Fig. 1 shows the experimental setup for combined frequency-domain PTR and luminescence (LUM) probing. Three semiconductor lasers with wavelengths 658 nm (80 mW; Mitsubishi ML120G21), and 670 nm (500 mW, Sony SLD1332V) were used as the sources of both PTR and LUM signals. A diode laser driver (Coherent 6060) was used for the lasers and was triggered by the built-in function generator of the lock-in amplifier (Stanford Research SR830), modulating the laser current harmonically. The laser beam was focused on the sample with a high performance lens (Gradium GPX085) to a spot size of approximately 150-170 μ m. The modulated infrared PTR signal from the tooth was collected and focused by two off-axis paraboloidal mirrors onto a Mercury Cadmium Telluride (HgCdTe or MCT) detector (EG&G Judson J15D12-M204-S050U). For the simultaneous measurement of PTR and LUM signals, a germanium window was placed between the paraboloidal mirrors so that wavelengths up to 1.85 μ m (Ge bandgap) would be reflected and absorbed, while infrared radiation with longer wavelengths would be transmitted. The reflected luminescence was focused onto a photodetector of spectral bandwidth 300 nm ~ 1.1 μ m (Newport 818-BB-20). A cut-on colored glass filter (Oriel 51345, cut-on wavelength: 715 nm) was placed in front of the photodetector to block laser light reflected or scattered by the tooth. For monitoring the modulated luminescence, another lock-in amplifier (EG&G model 5210) was used. Both lock-in amplifiers were connected to, and controlled by, the computer via RS-232 ports.

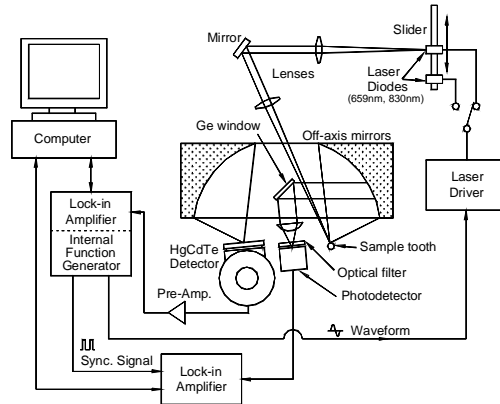


Fig. 1 Schematic diagram and a picture of experimental set-up for combined PTR and LUM monitoring.

Two kinds of experiments were performed. One was a frequency scan to examine the frequency dependence of the PTR and the LUM signals from 1 Hz to 1 kHz. The other type of experiment measured the PTR and the LUM signals along a spatial coordinate on the tooth surface at a fixed frequency.

2.1.2. Example 1: Deep sub-surface carious lesion in dentin

The horizontal cross-section of a mandibular central incisor with a large carious lesion on both interproximal surfaces is shown in Fig. 2(a). Fig. 2(b) is a view of the horizontal cross-section at a level indicated by the arrow in Fig. 2(a). It shows (high-lighted) the carious lesion involving most of the dentin, and a section of the pulp horn just beneath the dentin surface. The white area within the high-lighted region is actually dentin that is not highly mineralized since it is very near the pulp and contains a large number of tubules, much higher than dentin near the dentin-enamel junction (DEJ). The arrow in Fig. 2(b) shows the direction and extent of the laser scan across the intact side surface of the tooth corresponding to the arrow in Fig. 2(a). The spatial scan results with the 659-nm laser as a source modulated at 5 Hz are shown in Fig. 2(c). From the onset to the middle of the scan, the PTR amplitude is high (5×10^{-4} V range) over the region which is consistent with the presence of the deep sub-surface lesion at approx. 2.5 mm below the tooth surface. The PTR signal drops to ca. 5×10^{-5} V outside the carious region and rises slightly again close to the right edge of the tooth (a thermal-wave edge effect¹⁷). The LUM amplitude also shows similar structure but far less dramatic contrast than the PTR amplitude, a further indication of the non-depth-profilometric nature of modulated luminescence as signal strength is weighed equally from all sub-surface depths. The difference in sensitivity to the deep sub-surface lesion between PTR and LUM is that the PTR is more sensitive to deeper inhomogeneities than LUM even when sharp boundaries are involved. The low-frequency (< 100 Hz) insensitivity of the LUM phase, Fig. 2(d), to sub-surface dental structure has been noted earlier¹³.

2.1.3. Example 2: Enamel cracks

The tooth shown in Fig. 3(a) is healthy but there is a natural radial crack in the thick enamel as shown on the top-down cross-sectional plane of Fig. 3(b). The spatial scan results along the white arrow with the 659-nm laser at 5 Hz are shown in Fig. 3(c). Dashes in Fig. 3(b) have been added at the enamel-dentin junction to aid the eye. A sharp PTR amplitude peak and a shallow, broadened, LUM amplitude peak caused by the crack are shown around 2.8 mm from the scan onset coordinate point. PTR shows higher spatial resolution and contrast than LUM because the latter is more sensitive to scattered excitation light at the crack which broadens the region from which multi-scattered luminescence photons are collected. The PTR signal is primarily due to the thermal discontinuity in the cracked region which occurs along the actual crack configuration and is thus more representative of the actual crack extent. The fact that there are no significant changes in the PTR phase scan, indicates that thermal-wave flux disruption occurs mainly sideways as the laser beam sweeps across the walls of the crack, rather than impeding flux along the depth coordinate, a phenomenon well-known from Mirage-effect measurements in the non-destructive evaluation of cracks in engineering materials^{15,18}. Unfortunately, the expected small phase variation from the lateral thermal impedance represented by the crack wall is lost in the noise of Fig. 3(d), as the overall healthy tooth generates low PTR signals less than 10^{-4} V. It has been found that, as a rule, healthy and thick enamel generates small PTR and LUM amplitudes (< 0.1 mV). The LUM phase shows no contrast, consistently with the insensitivity of this signal channel to dental irregularities at low frequencies. In

summary, successful PTR detection of natural sub-surface cracks in teeth, also reported earlier⁵, depends on the size, orientation and depth of the crack. LUM detection is unpredictable and may possibly distort the geometric shape of the crack.

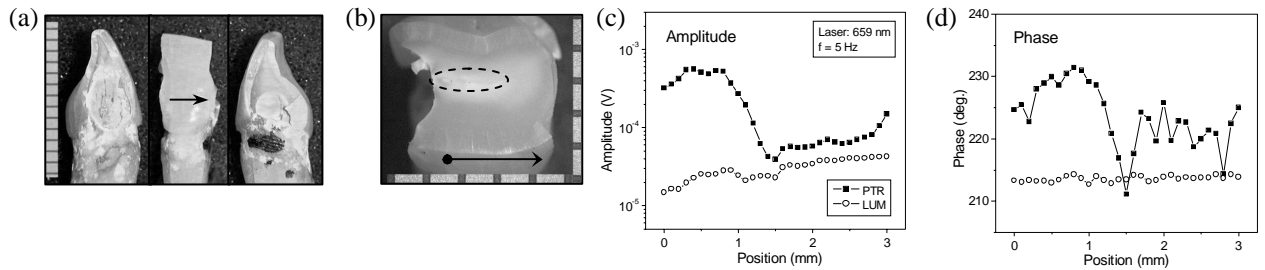


Fig. 2 Photographs and experimental results of the sample tooth having deep sub-surface carious lesion in dentin. (a) left, front, and right views of a mandibular incisor. (b) cross-section at the scan line at the level of the arrow in (a), highlighting a deep demineralized lesion (dotted region in the middle); (c,d) PTR and LUM amplitude and phase signals across the scan line at 5 Hz and 659 nm.

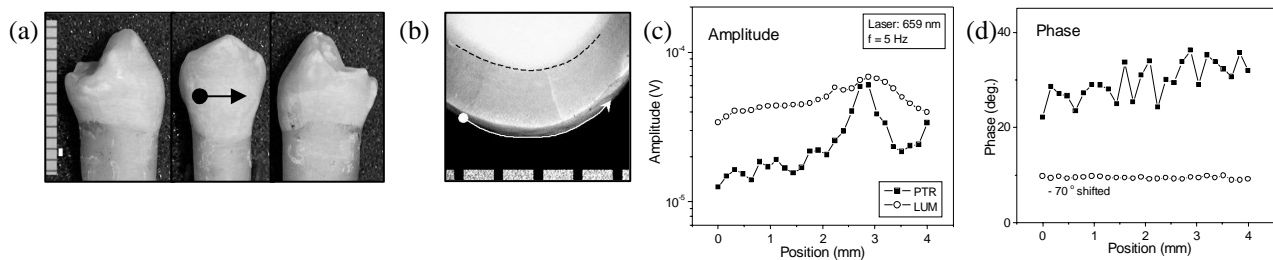


Fig. 3 Photographs and experimental results of a mandibular bicuspid with a radial enamel crack. (a) left, front, and right views of the tooth; (b) cross section at the scan level showing the radial crack. The DEJ is highlighted to aid the eye; (c,d) PTR and LUM amplitude and phase signals across the scan line at 5 Hz.

2.2. Statistical approach (diagnosis of pit and fissure caries)

Fifty two human teeth were examined to evaluate the diagnostic capabilities of FD-PTR and FD-LUM and were compared to DIAGNOdent, a device based on dc luminescence responses from optically excited enamel² as well as visual inspection and radiographs. After the measurements were completed, the teeth were sectioned. Histological findings were used as the gold standard to calculate and compare the sensitivity and the specificity of all the diagnostic methodologies used in this study.

Fig. 4 shows a mandibular second premolar illustrating the typical diagnostic ability of PTR and LUM. The tooth had a DIAGNOdent reading of maximum 10 and average visual inspection ranking of 2.2 indicating that a clinician would need to watch or monitor the fissures. There was no indication on the radiographs of any caries being present. Nevertheless, PTR and LUM signals, including all information from the amplitude and phase responses over the entire frequency scan (1 Hz ~ 1 kHz), indicated that F2 and F3 have caries into dentin. Histological observation results showed that this is, indeed, the case for these two points, as well as for point F1. The signals from fissure F1 show the influence that fissure geometry, angle of the mouth of the fissure, or the direction of the fissure base may have in the generation of PTR and LUM signals. The PTR amplitude of F1 in Fig. 4(f) is above the healthy band and the PTR phase in Fig. 4(g) also shows clear departure from the healthy band in the high frequency range. This case illustrates the depth profilometric abilities of PTR. Fig. 4(b) shows that the slanted carious fissure F1 was illuminated by the incident laser beam in such a way that the carious region formed a thin surface layer, succeeded by a much thicker healthy substrate enamel layer. In response, the phase of the PTR signal for F1, Fig. 4(g), falls within the healthy band at low frequencies as expected from the long thermal diffusion length which mostly probes the healthy enamel sub-layer with the carious surface layer as a perturbation to the signal. At high frequencies, however, the (short) thermal diffusion length lies mostly within the carious surface layer and, as a result, the PTR phase emerges below the healthy band above ca. 50 Hz and joins the phases of the carious spots F2 and F3. In principle, the frequency of departure from

the healthy band can be used to estimate the thickness of the carious surface layer. PTR and LUM curves of the healthy fissure F4 are located within the healthy band confirming the histological observations.

In order to assess PTR and LUM as caries diagnostic techniques and compare them (combined and separately) to other conventional probes, sensitivities and specificities were calculated at two different thresholds (D_2) and (D_3) as defined in Table 1 for all the diagnostic methods. While the PTR and LUM signals were taken from all 280 occlusal measurement points, only 1 or 2 points on each tooth were assessed by the other examination methods. Therefore, each calculation only used the corresponding measurement points. To create suitable criteria for assessing the carious state via PTR and LUM, the general characteristics of the respective signals and their converting equations, listed in Table 2 were used. Those characteristics were established from the experimental results of the frequency scans with carious and healthy tooth samples. In the case of the PTR amplitude, the shape of the frequency scan curve for the healthy spot on a log-log plot is almost linear from low frequency (1 Hz) to high frequency (1000 Hz), while unhealthy spots (demineralized surface, enamel caries or dentin caries) exhibit larger amplitude than healthy spots over the entire frequency range and a pronounced curvature with a “knee” at certain frequency ranges on the logarithmic plot. The PTR phase shape for the healthy spot on a linear (phase) - log (frequency) plot is almost linear across all frequencies (1 Hz ~ 1 kHz), while carious spots exhibit larger phases at low frequencies and large slopes, crossing the healthy phase range at intermediate frequencies. There is no difference in the LUM amplitude shape between healthy and carious spots. The shape of the amplitude curves is consistent throughout, decreasing from low to high frequencies. The LUM amplitude curves for unhealthy spots lie above the healthy band over the entire frequency range. The LUM phase shows slight differences between healthy points and carious points. In general, carious regions exhibit LUM phase lags slightly shifted above the healthy mean throughout the measured frequency range. Healthy spots may exhibit slight deviations, but only at the high frequency end (> 100 Hz).

Table 1. Diagnostic criteria for the Visual Inspection, DIAGNOdent, X-ray and Histological Observation

General Description of Levels of Caries	Visual Inspection (1~10)	DIAGNOdent (0~99) [3]	Radiograph	Histological Observation
D_0 : Intact			Healthy: Indicating no sign of demineralization	Sound enamel or Healthy fissure
D_1 : no caries, or histological enamel caries limited to the outer half of the enamel thickness	1 ~ 2 Incipient or Healthy Fissures Observe & Monitor	0-4	Enamel caries under 1/2 the distance to DEJ	Demineralized fissure but solid enamel base; very good enamel thickness to the pulp; at least 1/2 thickness of enamel remains intact
D_2 : histological caries extending beyond the outer half, but confined to the enamel	2 ~ 5 Fissures are suspect. Fissure Sealant recommended	4.01 ~ 10	Enamel caries greater than 1/2 the distance to DEJ	Demineralized fissure but solid enamel base
D_3 : histological dentinal caries limited to the outer half of the dentin thickness	6 ~ 8 Restore the Fissure with direct placed restoration	10.01 ~ 18	Dentin caries	Caries into dentin
D_4 : histological dentinal caries extending into the inner half of dentin thickness	9 ~ 10 Deep Dentin Caries Large carious lesions	> 18.01		

Table 2. Characteristics of frequency scan curves of PTR and LUM

Signal	General characteristics	Converting equation to determine numeric ranking
PTR amplitude	The shape for a healthy spot in log-log plot is almost linear from low frequency (1 Hz) to high frequency (1000 Hz). Unhealthy (demineralized surface, enamel caries or dentin caries) spots show greater amplitude at all frequency ranges compared to healthy spots. Unhealthy spots show a curvature (greater than healthy spots) in the frequency range of 10 ~ 100 Hz in a logarithmic plot.	(slope at low frequency) – (slope at high frequency) average of 4 frequencies
PTR phase	The shape for the healthy spot in log (freq.) - linear (phase) plot is almost linear from low frequencies (1 Hz) to high frequencies (1000 Hz). Unhealthy spots show higher phase at low frequency range and the reverse at the high frequency range than healthy spots.	(average of phases at 2 low frequencies (1, 6.68 Hz)) – (average of phases at 2 high frequencies (211.35, 1000 Hz))
LUM amplitude	Both healthy and unhealthy spots show same shape: higher amplitude at low f than at high f. Unhealthy spots show greater amplitude than healthy ones.	average at 3 frequencies (1, 211.35, 501.18 Hz)
LUM phase	High frequency range (> 100 Hz) only, unhealthy spots show larger phase than healthy ones.	one phase signal at high frequency (501.18 Hz)

Establishing the mean values for PTR amplitude and phase, and LUM amplitude and phase from all the healthy smooth surface points on the tooth samples allowed us to examine the behavior of healthy tooth structure without the influence of fissure geometry or the effects of varying enamel thickness in the fissure. A series of mean values and standard deviations vs. frequency curves were developed for each signal and plotted for each tooth. This allowed comparison of the behavior of each probed point to a healthy smooth surface area.

Using these features, characteristic (converting) equations were generated from the plots to yield numeric values defining the state of the teeth as listed in Table 2. In addition, out of the entire frequency scan, each signal (PTR and LUM amplitude and phase) was examined at 3 or 4 frequencies whether it deviated from the healthy norm band, and the number of points that deviated from this band was counted. After calculating all these values, each number group was normalized so that the assigned numbers in each group had a value between 0 for intact teeth and 1 for the worst case of caries. Then these normalized numbers were added and used to evaluate the probed spots. Finally, one value per each measurement point was recorded which included all available information of the frequency response. The thresholds of D_2 and D_3 were determined by trial and error to comply with the histological observations as closely as possible.

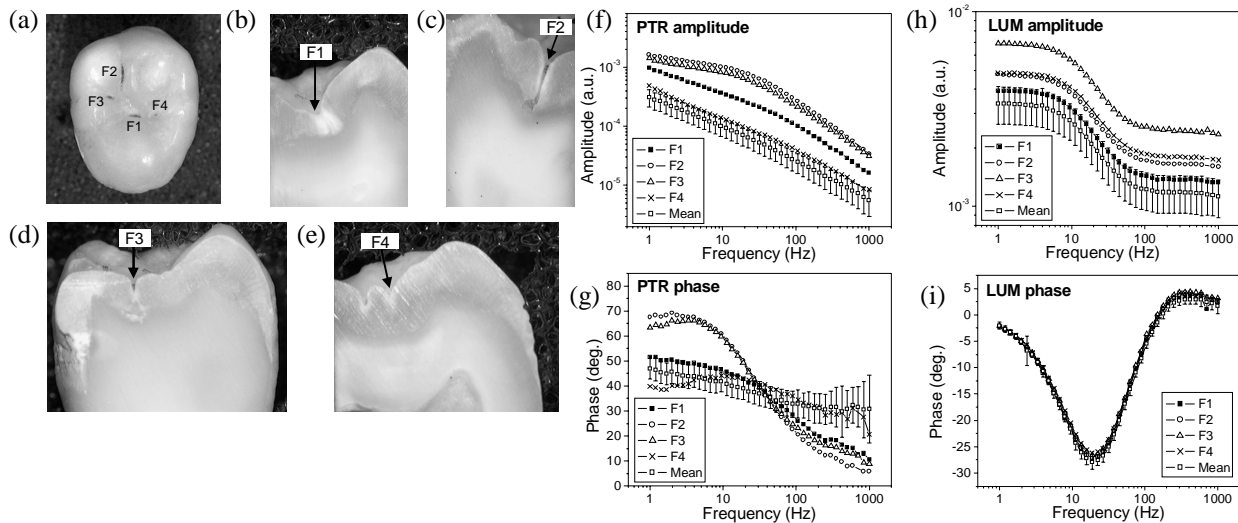


Fig. 4 A carious tooth sample and its PTR and LUM signals using 659-nm excitation. (a) occlusal view of the tooth; (b-e) cross sectioned view of each measurement point, F1, F2, F3 and F4; (f,g) PTR and (h,i) LUM amplitude and phase frequency scans at all the measurement points with the healthy mean value and population-weighted standard deviation.

Table 3. Sensitivities and specificities at the caries level of enamel (D_2) and the caries level of dentin (D_3) for various examination methods

Examination method	Sensitivity threshold (D_2/D_3)	Specificity threshold (D_2/D_3)	Size of sample (# of points)
PTR and LUM combined	0.81 / 0.79	0.87 / 0.72	280
PTR only	0.69 / 0.52	0.86 / 0.72	280
LUM only	0.61 / 0.58	0.81 / 0.77	280
Visual Inspection	0.51 / 0.36	1.00 / 1.00	52
Radiograph	0.29 / 0.36	1.00 / 0.85	52
DIAGNOdent	0.60 / 0.76	0.78 / 0.85	131

The results of the statistical analysis are given in Table 3. Using the combined criteria of PTR and LUM, the highest sensitivities and specificities, 0.81 and 0.87, respectively, were calculated at the D_2 threshold among all the examination methods. In the cases of PTR-only or LUM-only criteria, sensitivities are between 0.52 and 0.69, while specificities are relatively higher, between 0.72 and 0.86. In a manner similar to other findings^{3,19}, visual inspection resulted in poor sensitivities (0.51 at D_2 and 0.36 at D_3) and particularly high specificities (1.00 at both thresholds). Radiographs also exhibited poor sensitivities (0.29 at D_2 and 0.36 at D_3) and high specificities (1.00 at D_2 0.85 at D_3). The continuous (dc) luminescence method (DIAGNOdent) showed sensitivities of 0.60 at D_2 and 0.76 at D_3 ; specificities were 0.78 at D_2 and 0.85 at D_3 . From Table 3 it should be noted, however, that a relatively small subset of all measurement spots

was used for obtaining the visual and radiographic statistics, compared to the much more comprehensive sample sizes used for the other methods, especially for PTR and LUM. In addition, DIAGNOdent measurements were performed with that instrument's fiber-optic waveguide, whereas LUM and PTR measurements used direct incidence of the light on the tooth surface and were subject to variable incidence solid angle limitations.

2.3. Interproximal lesion detection

Very recently, interproximal lesions have been examined by PTR and LUM. Lesions were created either with very fine burs, and artificial caries agents in the contact area of a pair of teeth which were mounted on LEGO bricks. This set up allowed the teeth to be separated and remounted onto the exact position after creating the artificial lesions. Intact or treated human teeth were examined with PTR at various relative angles of the laser source and the detector using a specially designed rotational stage. Dental bitewing radiographs were also taken to determine whether dental X-rays could identify these defects.

Extracted human teeth were mounted on LEGO bricks so that a pair of teeth was in point contact, Fig. 5(a). The samples with mechanical holes were stored in saline solution and removed from the container just before the experiments, rinsed thoroughly with tap water for more than 20 seconds, and then left in air for 20 minutes to be dried properly. After the experiments, these samples were immediately placed in the container. However, for long term treatments (hours to days) of samples with a demineralization-remineralization solution, after several times of testing, humidity control was found to be important in reproducing signal baselines because teeth would be exposed in the dry air for a long time during treatment. To ensure similar humidity environments for all samples, a humid tight box was used with distilled water in Petri dishes for providing samples humidity without direct water contact. Each pair of teeth was mounted on the LEGO bricks and was scanned at 30Hz from the left to right across the interproximal contact spot as shown with arrows in Fig. 5(a) and Fig. 6(a). These samples were scanned and radiographed at every step of machining or treatment with an artificial caries agent.

In order to see if small artificial holes could be detected by PTR and/or LUM, a ¼ mm fine dental bur was used to make holes with approximately ¼ mm depth on the sides of both teeth at the contact location. As shown in Fig. 5(b), the left side hole was deeper than that on the right side, so it could be visible on the X-ray image. PTR and LUM signals are shown in Fig. 5(c). PTR amplitudes are clearly higher after the sequential drilling of holes, to the left and to the right of the contact point at 1.2~2.3mm. PTR phases showed big changes at around the holes at 1.5~2.5mm, too. In the PTR phase, some signal changes also appeared at regions away from the drilled holes, 0~1.5mm and 2.5~4mm. The PTR amplitude also showed similar behavior. The LUM amplitude and phase didn't show clear differences around the holes because the LUM is essentially a surface phenomenon while the PTR delivers deep sub-surface information⁷. LUM amplitude and phase showed slight decreases at all scans, possibly because LUM is very sensitive to humidity changes.

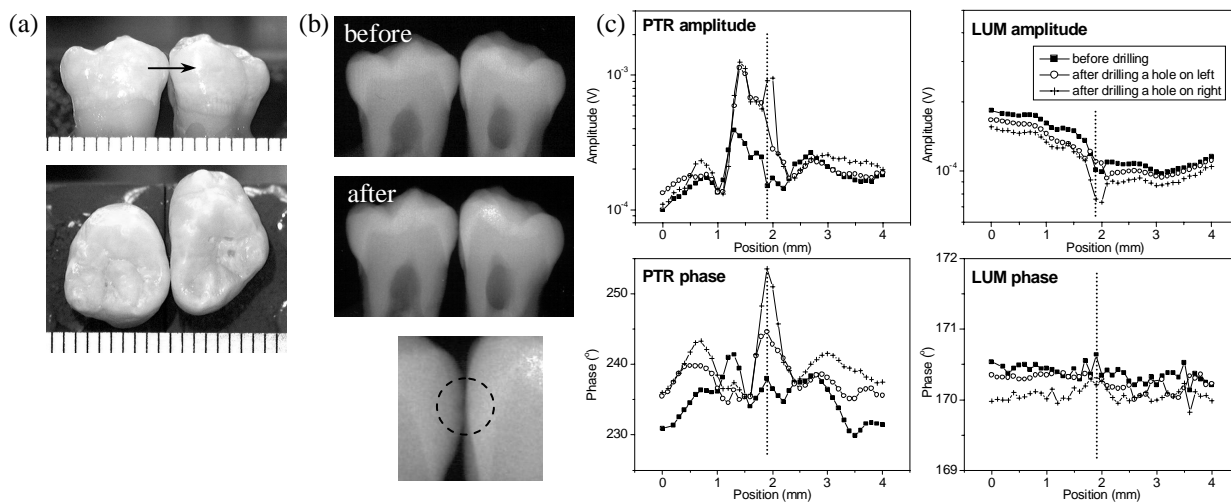


Fig. 5 Photographs and experimental results of an interproximal artificial lesion (mechanical hole) detection. (a) front, and top views of the teeth; (b) X-rays before and after drilling holes; (c) PTR and LUM amplitude and phase signals across the scan line at 30Hz.

Another sample set was treated by a demineralization-rem mineralization solution (2.2 mM Potassium Phosphate, monobasic (KH_2PO_4), 50 mM Acetic acid (NaOAc), 2.2 mM of 1M Calcium Chloride (CaCl_2), 0.5 ppm Fluoride (F^-), and Potassium Hydroxide (KOH) for balancing the pH at 4~4.5). Fig. 6(b) shows X-rays before and after treatment for 80 hours and 170 hours, but X-rays appear to be insensitive to the treatment. On the contrary, both PTR amplitude and phase showed clearly monotonic increases after each treatment while LUM was nearly insensitive but for the slight rigid shift (decrease) of the curves across the scanned region due to humidity changes.

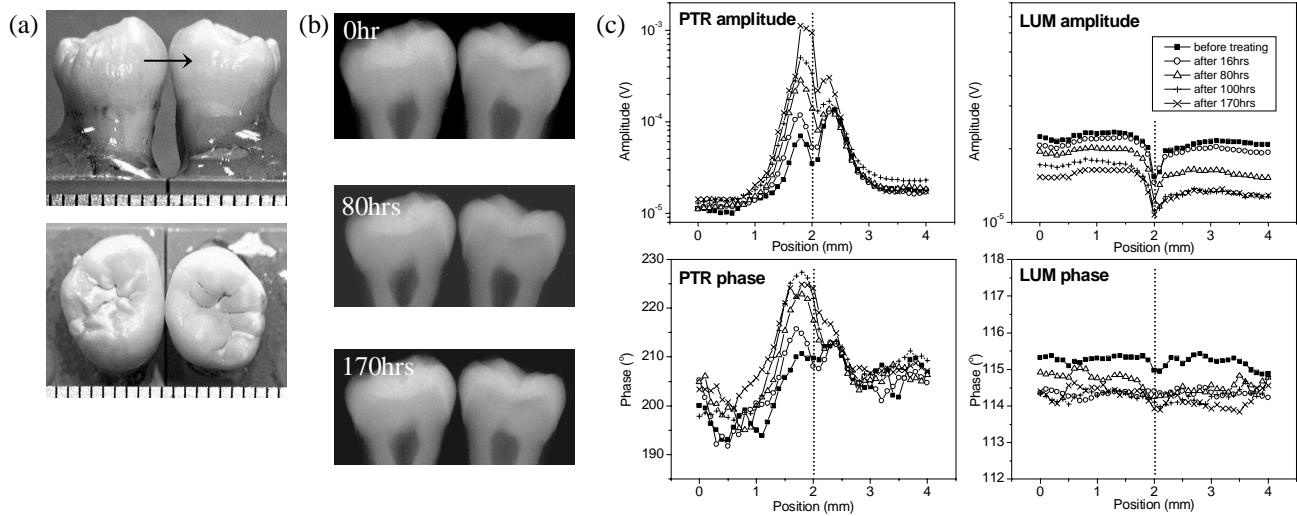


Fig. 6 A pair of teeth with an interproximal artificial lesion (demineralization-rem mineralization treatment) (a) front, and top views of the teeth; (b) X-rays before and after treatment for 80 hrs and 170 hrs; (c) PTR and LUM amplitudes and phases across the scan line at 30Hz.

3. FREQUENCY DOMAIN BIOACOUSTOPHOTONIC IMAGING OF SOFT TISSUES

3.1. Theoretical analysis of frequency-domain bioacoustophotonic signal generation

A mathematical model developed to study the laser-induced generation of acoustic waves in turbid media includes both the scattering and absorption effects, and assumes the diffusion approximation of the radiative transfer equation²⁰ to describe the distribution of optical radiation in tissue. The geometry of optical excitation for a one-dimensional model representing a solid light-scattering layer positioned within a surrounding fluid is shown in Fig.7.

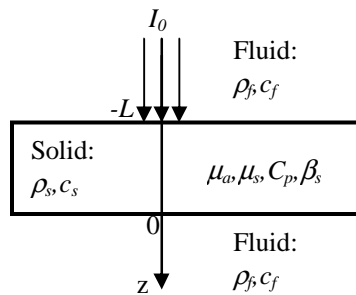


Fig. 7 One-dimensional geometry of photothermoacoustic effect in a light-scattering sample.

The surrounding fluid represents an acoustic coupling medium between the probed solid and the transducer and is assumed to have the physical properties of water and occupies the spatial regions $-\infty < z \leq -L$ and $0 \leq z < \infty$. The fluid is characterized by density ρ_f and speed of sound c_f . The solid layer has thickness L , density ρ_s , speed of sound c_s , specific heat at constant pressure C_{ps} , optical absorption μ_a and scattering μ_s coefficients, bulk modulus K_s and isobaric volume

expansion coefficient β_s . Analysis of acoustic wave generation in turbid media requires solution of a coupled boundary value problem involving equations for the radiative photon transport, the heat conduction and the acoustic pressure waves constrained by appropriate boundary conditions²¹⁻²⁴. For a harmonic optical source, it is convenient to use frequency domain representations of the radiant fluence $\Psi(z, \omega)$, temperature $\theta(z, \omega)$ and acoustic pressure $P(z, \omega)$ that can be related to respective time-domain counterparts via a Fourier transform pair. A closed form solution can be derived for a one-dimensional geometry (Fig. 1) using the diffusion-wave transport equation:

$$\frac{\partial^2}{\partial z^2} \Psi_d(z, \omega) + \sigma_p^2 \Psi_d(z, \omega) = -\frac{S_0(z, \omega)}{D} \quad (1)$$

where Ψ_d is the diffuse scattered photon fluence, $\sigma_p^2 = (i\omega - c\mu_a)/D$ is the diffuse photon wave number, $D = c/3(\mu_a + \mu_s')$ is the photon diffusion coefficient, $\mu_s' = \mu_s(1-g)$ is the reduced scattering coefficient, g is the scattering anisotropy factor, c is the speed of light in a sample, and the source function $S_0(z, \omega) = \mu_s I_0 c (\mu_t + g\mu_a) / (\mu_t - g\mu_s) \exp(-\mu_t(z+L))$, where I_0 is the laser fluence and $\mu_t = \mu_a + \mu_s$. Equation (1) must be complemented by boundary conditions for photon fluxes at both interfaces $z = -L$ and $z = 0$:

$$\begin{aligned} \Psi_d(-L, \omega) - A \frac{\partial}{\partial z} \Psi_d(-L, \omega) &= -3\mu_s g A I_0 \\ \Psi_d(0, \omega) + A \frac{\partial}{\partial z} \Psi_d(0, \omega) &= 3\mu_s g A I_0 e^{-\mu_t(z+L)} \end{aligned} \quad (2)$$

where $A = 2D(1 + r_{21})/c(1 - r_{12})$, r_{21} is the internal reflection coefficient, defined as the ratio of the upward-to-downward hemispherical diffuse photon fluxes. The total radiant fluence Ψ is composed of diffused Ψ_d and coherent Ψ_c fields: $\Psi(z, \omega) = \Psi_d + \Psi_c$, which stimulates the photothermal effect described by the heat conduction equation:

$$\frac{\partial^2}{\partial z^2} \theta_s(z, \omega) - \sigma_s^2 \theta_s(z, \omega) = -\frac{\mu_a \Psi(z, \omega)}{\kappa_s} \quad (3)$$

where $\theta_s(z, \omega)$ is the thermal-wave function, $\sigma_s^2 = (i\omega/\alpha_s)$, α_s and κ_s are, respectively, the thermal diffusivity and conductivity of the sample. The heat conduction equation (3) must be accompanied by the continuity conditions for temperature and heat flux at the fluid-solid interfaces:

$$\begin{aligned} \theta_f(-L, \omega) &= \theta_s(-L, \omega) \\ \kappa_s \frac{\partial}{\partial z} \theta_s(-L, \omega) &= \kappa_f \frac{\partial}{\partial z} \theta_f(-L, \omega) \\ \theta_f(0, \omega) &= \theta_s(0, \omega) \\ \kappa_s \frac{\partial}{\partial z} \theta_s(0, \omega) &= \kappa_f \frac{\partial}{\partial z} \theta_f(0, \omega) \end{aligned} \quad (4)$$

Finally, the spectrum $P(z, \omega)$ of laser-induced pressure waves in the surrounding fluid can be found from Helmholtz equations introducing the displacement potential $\phi_s(z, \omega)$ and the scalar potential $\zeta_f(z, \omega)$ of the fluid motion:

$$\begin{aligned} \frac{\partial^2}{\partial z^2} \phi_s(z, \omega) + k_s^2 \phi_s(z, \omega) &= \frac{K_s \beta_s}{\rho_s c_s^2} \theta_s(z, \omega) \\ \frac{\partial^2}{\partial z^2} \zeta_f(z, \omega) + k_f^2 \zeta_f(z, \omega) &= 0 \end{aligned} \quad (5)$$

where k_s and k_f are the acoustic wave numbers in the solid and fluid, respectively. Equations (5) are subject to boundary conditions for stress and displacement velocity:

$$\begin{aligned} \rho_s c_s^2 \frac{\partial^2}{\partial z^2} \phi_s(0, \omega) - K_s \beta_s \theta_s(0, \omega) &= i\omega \rho_f \zeta_f(0, \omega) \\ \rho_s c_s^2 \frac{\partial^2}{\partial z^2} \phi_s(-L, \omega) - K_s \beta_s \theta_s(-L, \omega) &= i\omega \rho_f \zeta_f(-L, \omega) \\ i\omega \frac{\partial}{\partial z} \phi_s(0, \omega) &= \frac{\partial}{\partial z} \zeta_f(0, \omega) \\ i\omega \frac{\partial}{\partial z} \phi_s(-L, \omega) &= \frac{\partial}{\partial z} \zeta_f(-L, \omega) \end{aligned} \quad (6)$$

The solution of the coupled boundary-value problems (1)-(6) can be derived in closed form for one-dimensional geometry and was given in detail elsewhere²⁵. The small-amplitude acoustic pressure change in the fluid is related to velocity potential as: $P(z,w) = -i\omega\rho_f\zeta_t(z,\omega)$ and can be written using the solution of Eqs.(5),(6) as:

$$P(z, \omega) = -i\omega\rho_f G e^{ik_f(z+L)} \quad (7)$$

where the complex valued constant G depends on the modulation frequency ω , the sample optical and thermal properties and thickness L .

Theoretical simulations were performed for the simple case of a solid turbid layer immersed in water. Three input parameters, the optical absorption coefficient, optical scattering coefficient and thickness of the solid were changed independently for each simulation to analyze the time-domain PTA signal generation. Equation (7) was used to calculate the laser-induced acoustic field within a user-selected frequency range. The time-domain response was reconstructed from the computed spectrum using inverse Fourier transform. Experimental verification was conducted using a heterodyne FD-PTA profilometric system described in our earlier work²⁵ for the same range of modulation frequencies. Fig. 8 demonstrates theoretical simulations and experimental results obtained for a tissue phantom prepared from plastisol mixed with different concentrations of a plastic color to introduce absorption at the 1064 nm.

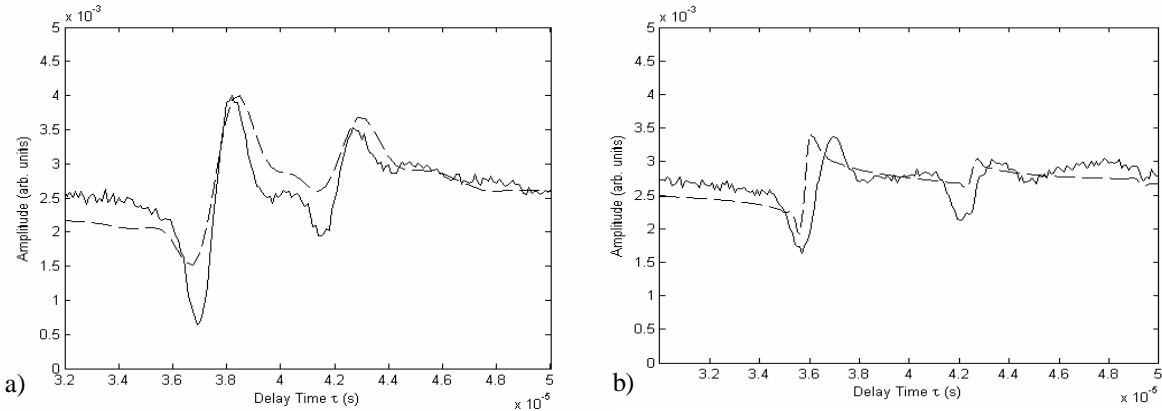


Fig. 8 Measured and calculated PTA fields obtained for a solid phantoms with different absorption coefficient $\mu_a=0.95 \text{ cm}^{-1}$ (a) and $\mu_a=0.65 \text{ cm}^{-1}$ (b). Phantom thickness was 6.87 mm (a) and 8.2 mm (b).

The solid lines in Fig. 8 are the experimental results of a single spatial point cross-correlation (“delay”) time scan for phantoms with absorption coefficient $\mu_a = 0.95 \text{ cm}^{-1}$ (Fig. 8a) and $\mu_a = 0.65 \text{ cm}^{-1}$ (Fig. 8b), positioned at the distance of 5.4 cm from an ultrasonic transducer. The frequency was varied in the range from 0.1 MHz to 1 MHz. The frequency-domain simulated results were calculated by substituting thickness (6.87 and 8.2mm), detection distance, material properties, and frequency variation range into Equation (7). The corresponding time-domain numerical acoustic pressure fields exhibited good agreement with the experimental results. Due to the large size of the laser beam (~ 4 mm) and the additional divergence due to scattering inside the imaging layer, the PTA behavior was expected to be very similar to the 1D situation and to be adequately interpreted by the 1-D theory, as observed. These theoretical simulations demonstrate that the time-domain PTA response can be reconstructed from the frequency modulation scans and inverse Fourier transforms applied to the recorded PTA spectra. Although such measurements can be conducted using a standard lock-in amplifier, recording of frequency scans is very time consuming and would be impractical in real-life imaging applications. Our implementation of the FD-PTA imaging system employs rapid frequency swept (chirped) modulation of laser radiation, and a signal processing algorithm that relates spectrum of the recorded PTA signals to the depth of sub-surface chromophores in tissue. The depth information in a LFM detection algorithm can be assessed by mixing the PTA signal with a replica of the modulation chirp. For example, assume that the acoustic pressure signal $P(t) = P_0 \exp[i(2\pi f(t-\tau)t + \varphi_p)]$ is generated from a single subsurface chromophore. Here P_0 is the amplitude, φ_p is the initial phase, $f(t) = f_0 + bt$ is the modulation chirp with frequency increase rate b , and $\tau = z_{ch}/c_a$ is the delay time of acoustic wave propagation from the depth z_{ch} with speed of sound c_a . Mixing $P(t)$ with a reference chirp $R(t) = \exp[i2\pi f(t)t]$ and removing the sum frequency components in a low-pass filter (LPF), the combined signal becomes:

$$V(t) = \langle P(t)R(t) \rangle = \frac{P_0}{2} e^{-i(2\pi b\tau t - \phi_p)} \quad (8)$$

The spectrum of the product contains the characteristic frequency $f_{ch} = b\tau = b(z_{ch}/c_a)$ proportional to the chromophore depth z_{ch} . In other words, the spectral content of $V(t)$ contains depth profilometric information about the sub-surface chromophores. Since a weak PTA signal is normally contaminated by a significantly higher noise component, a lock-in detection technique can be employed to examine specific frequency ranges relevant to particular depths. Alternatively, a cross-correlation detection with time-averaging can be used to increase SNR of PTA measurements.

3.2. Experimental apparatus of the FD-PTA imaging system

Application of linear frequency modulated signals in radar (and sonar) instrumentation has found widespread use as an alternative way to increase detection range while avoiding generation of high peak power pulses of radio waves^{26,27}. The optical analog of this technology was adopted in frequency-domain optical coherence tomography (OCT) for microscopic imaging of near-surface tissue structures^{28,29}. Despite certain similarities in signal processing, those technologies differ from FD-PTA significantly by the fact that they detect echo response rather than energy locally converted from optical flux to acoustic pressure wave via the thermoelastic effect. Our implementation of the FD-PTA imaging system is shown in Fig. 9.

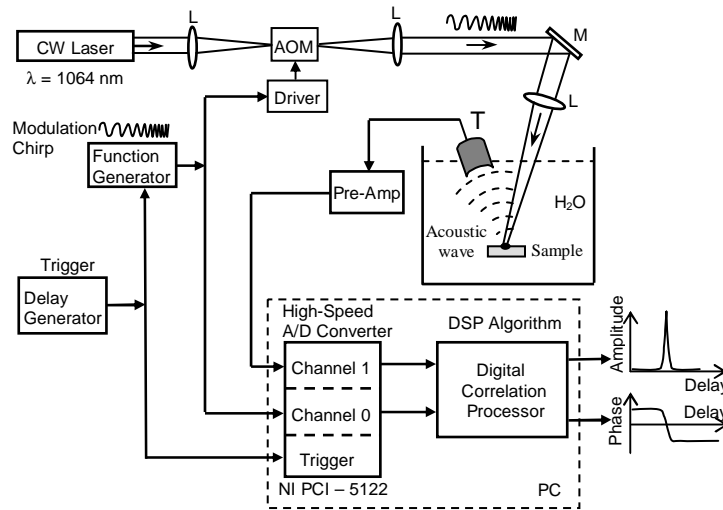


Fig. 9 Block diagram of the FD-PTA imaging system and signal acquisition schematics.

It features a CW fiber laser (IPG Photonics) at the wavelength 1064 nm, an acousto-optic modulator (Neos Technologies) which is driven by signals from a function generator (Stanford Research Systems, DS345) and a focusing ultrasonic transducer (Panametrics) immersed in a water container for acoustic coupling. A test sample is positioned in water at the focal distance from the transducer. Optical radiation is modulated continuously by LFM waveforms in the range 1 MHz – 5 MHz and 1 ms repetition time. Modulation signal and data acquisition are triggered by a delay generator (Stanford Research Systems, DG535) and two signals (transducer voltage and reference chirp) are digitized simultaneously using a high-speed analog-to-digital converter (ADC) (National Instruments, PCI-5122) capable of maximum sampling rate of 10^8 samples/sec. To process the acquired PTA signals, a software algorithm was designed and implemented, which employs digital correlation processing with respect to in-phase and quadrature modulation waveforms. This program simulates two virtual reference channels containing two chirps: a replica of the laser modulation and a chirp with 90-degree phase-shift introduced by a Hilbert transform. The subsequent processing stages compute the cross-correlation of two reference waveforms with the signal received by an acoustic transducer. Low-pass filters recover in-phase V_I and quadrature V_Q components of the signal and, finally, amplitude and phase are computed as:

$$A(\tau) = (V_I^2 + V_Q^2)^{1/2} \quad \text{and} \quad \phi(\tau) = \tan^{-1}(V_Q/V_I), \quad (9)$$

where τ is the delay time of reference chirps which can be varied within a pre-determined range. Since digital mixing and low-pass filtering effectively suppress all signals incoherent with a reference, the resulting amplitude is non-zero only for delays matching the arrival time of frequency modulated acoustic waves from a test sample.

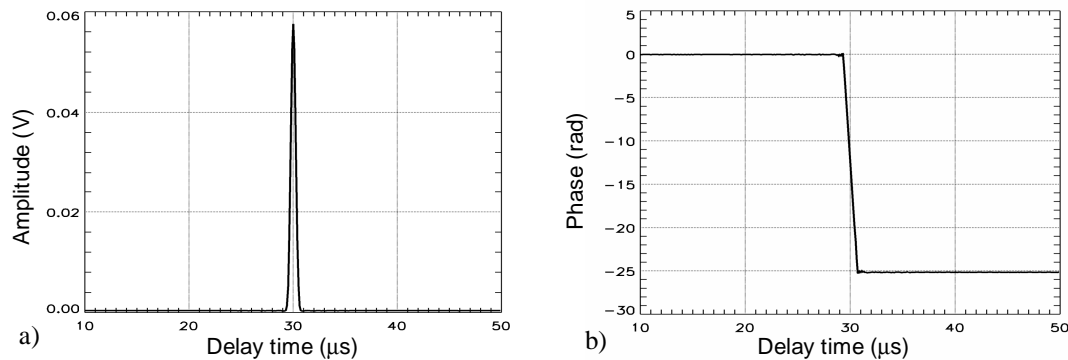


Fig. 10. Autocorrelation function amplitude (a) and phase (c) for a generator chirp signal delayed by 30 μs .

Plots in Fig. 10a and 10b show typical amplitude and unwrapped phase data for a noise-free chirp signal from a function generator delayed by 30 μs that simulates a PTA response. In the case of tissue which may include multiple discrete chromophores and background noise, the PTA signal is composed of a set of acoustic chirps with various amplitudes and delay times proportional to their depth. Therefore, demodulated amplitude data for a real tissue sample contain multiple peaks corresponding to different depths of tissue chromophores. Since chirp modulation is continuous, the PTA signal is averaged over multiple chirps and multiple scans to increase SNR. When the laser beam is scanned in the lateral direction, a 2-D slice PTA image can be reconstructed from consecutive depth (equivalent: time delay) scans. The depth resolution is determined by the width of the auto-correlation function which depends on the frequency sweep rate b . The phase data may be used for depth profilometry and imaging as well, however the system noise contaminates in-phase and quadrature channels resulting in numerous discontinuities of the phase at $\pm\pi$ unrelated to the actual PTA signal. To take advantage of the phase channel, additional signal conditioning is required to ensure unambiguous phase measurements.

3.3. FD-PTA imaging of tissue phantoms and *ex-vivo* specimens

A series of test measurements with plastisol phantoms simulating tissue optical properties and *ex-vivo* tissue samples (chicken breast with embedded gel chromophores) were conducted to assess the depth-profilometric and imaging capabilities of the FD-PTA system. A focusing acoustic transducer was used with the focal distance of 25.4 mm and peak sensitivity at 3.5 MHz. A high-frequency transducer provides superior spatial resolution because the width of auto-correlation function is inversely proportional to the chirp bandwidth. In our experiments, width of the auto-correlation function was equal to 0.5 μs (FWHM), which translates into spatial resolution approximately 0.7 mm (assuming the speed of sound $c_s = 1.48 \times 10^5 \text{ cm/s}$). Fig. 11 shows an example of FD-PTA imaging of a planar absorbing inclusion (absorption coefficient $\mu_a = 4.2 \text{ cm}^{-1}$) positioned 6.3 mm deep inside a phantom with the reduced scattering coefficient $\mu_s' = 1.3 \text{ cm}^{-1}$ and the ambient absorption $\mu_a = 0.5 \text{ cm}^{-1}$. The top surface of phantom (1) and the sub-surface inclusion interface (2) can be clearly visible as bright lines on the image. This image also reveals that acoustic waves reflected from mechanical discontinuities in the media appear as secondary sources in the PTA image. Arrow 3 indicates an artificial air gap under the inclusion which creates an acoustic impedance mismatch on the back surface.

The next important step on the way to clinical applications of the FD-PTA technique is characterization of the system performance with real tissue specimens. A suitable model adequately representing optical and mechanical properties of human tissue is a chicken breast specimen with artificially embedded optical inhomogeneities simulating a cancerous tumor. An example of a two-dimensional FD-PTA slice image with two embedded gel inclusions with $\mu_a = 4 \text{ cm}^{-1}$, positioned 3 mm and 7 mm below the tissue surface is demonstrated in Fig. 12a. The position of inclusions is labeled as (I) and a black ink marker (M) indicates the tissue surface.

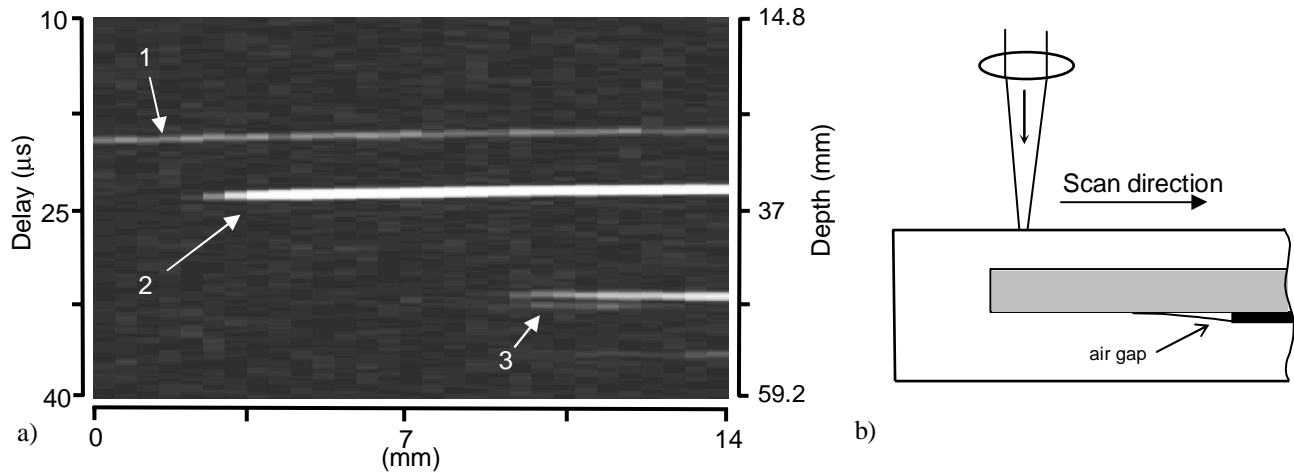


Fig. 11 A FD-PTA depth image of planar light-absorbing inclusion ($\mu_a = 4.2 \text{ cm}^{-1}$) imbedded in a test phantom ($\mu_s = 1.3 \text{ cm}^{-1}$, $\mu_a = 0.5 \text{ cm}^{-1}$) and scanning geometry (b). Arrows indicate: 1 – phantom surface, 2 – top surface of the inclusion, and 3 – artificial air gap under the inclusion.

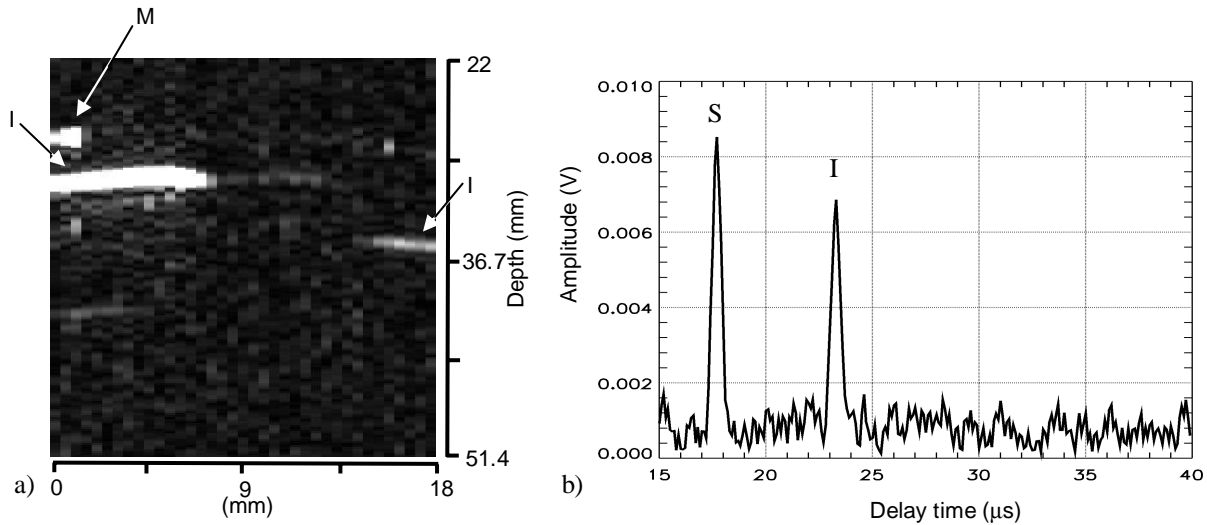


Fig. 12 FD-PTA imaging of chicken breast tissue: a) – chicken breast with two similar inclusions (absorption coefficient $\mu_a = 4 \text{ cm}^{-1}$) positioned at different depths; b) – a single point depth scan for a deep ($9 \pm 1 \text{ mm}$) inclusion in chicken breast. Arrow in the images: M – black ink marker on the tissue surface, I – imbedded inclusions, S- surface.

The top surfaces of inclusions appear as thin bright lines on the image at different delay times. Their position can be clearly identified and measured in the FD-PTA image, even though the amplitude of signal from the deeper inclusion is significantly reduced. A relatively deep subsurface inclusion ($9 \pm 1 \text{ mm}$) in chicken breast is shown in Fig. 12b which represents a single spatial point measurement averaged over multiple scans to reduce noise floor. These studies are currently being extended to deeper inclusions and to three-dimensional imaging using x-y scans. Although directly comparable information is scarce, there is evidence that state-of-the-art biomedical pulsed photoacoustic systems can “see” sub-surface inhomogeneities in tissues at *ca.* 1 cm below the surface with a SNR of $\sim 1.0 - 1.5$ ³⁰. The sub-surface peak of Fig. 12b shows a far superior SNR and feature sharpness. It is encouraging that this is not an upper limit of the FD-PTA technique, because the SNR can be further improved with suitable signal averaging, wavelength optimization and transducer redesign, a promise for the detection of deep ($\gg 1 \text{ cm}$) sub-surface optical inhomogeneities. Finally, preliminary tests with *in-vivo* tissue samples have been carried out to examine the sensitivity of the FD-PTA system to sub-surface chromophores typical to human tissue (epidermal melanin, blood vessels etc). A two-dimensional FD-PTA scan of an index finger of a healthy volunteer is shown in Fig. 13. The PTA signal from the finger surface is generated by light absorption in the epidermis while a discrete blood vessel appears as a localized increase in signal

amplitude below. The separate contributions of the skin surface (S) and a blood vessel (BV) are shown in Fig. 13b which represents a single depth scan recorded at the blood vessel position identified in the 2-D image.

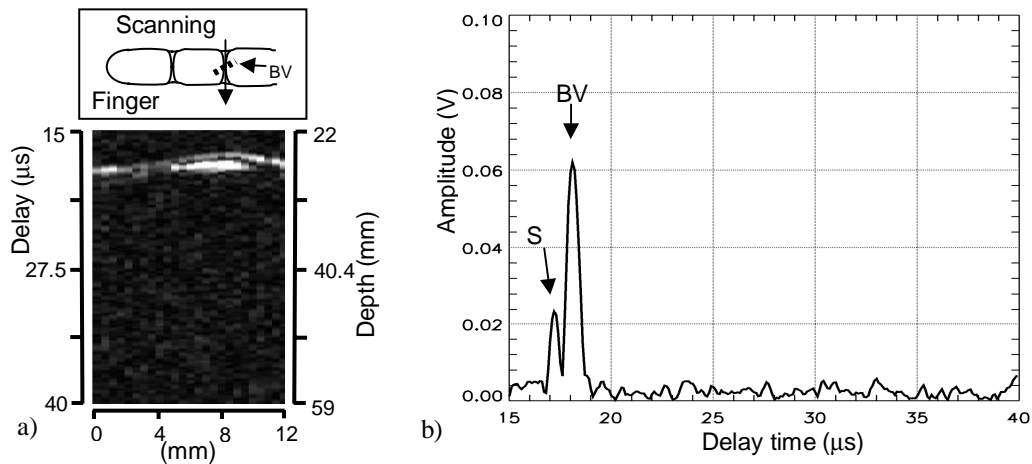


Fig. 13 A FD-PTA image of an index finger *in-vivo* (a) and a 1-D profile of amplitude recorded at the blood vessel position. Arrows on the plot: S – finger surface, BV – blood vessel.

4. CONCLUSIONS

In conclusion, trends in biothermophotonics and bioacoustophotonics away from pulsed laser detection and in frequency-domain depth-profilometric applications have been presented in two major areas of application: hard and soft tissue instrumentation and diagnostics. With major advantages in SNR compared to broadband detection techniques, natural defect such as a deep (longer than 2 mm) sub-surface carious lesions in dentin, invisible cracks and sub-surface demineralization have been shown to be detectable by biothermophotonic measurements using PTR and LUM. The combined PTR/LUM approach yielded a statistical sensitivity higher than state-of-the-art dental diagnostic methods, visual inspection and X-rays, and a specificity comparable to that of dc luminescence diagnostics, with DIAGNOdent. PTR has also been shown to be able to detect the artificial interproximal lesions which are difficult or impossible to diagnose visually or radiographically. Frequency domain photothermoacoustic imaging systems have been described for noninvasive imaging of biological tissues. The linear frequency modulated (chirped) optical excitation coupled with coherent signal processing provide dual channel (amplitude and phase) imaging capabilities and improved signal-to-noise ratio compared to pulsed photoacoustic methods. Bioacoustophotonic depth-profilometric imaging can be used to perform sub-surface slice-by-slice image reconstruction from operator-determined, precisely-controlled depths. It exhibits superior SNR at comparable depths with pulsed laser photoacoustics and may be applicable to biomedical imaging of blood rich tissue as in the case of sub-surface cancerous tumors.

ACKNOWLEDGMENTS

The support of Materials and Manufacturing Ontario (MMO) and of the Natural Sciences and Engineering Research Council of Canada (NSERC) through a CHRP Grant is gratefully acknowledged. S. Abrams, K. Kulkarni, W. Whelan, L. Nicolaidis, C. Feng and G. Spirou are acknowledged for valuable contributions in many aspects of several years of the development of the fields of frequency-domain biothermophotonics and bioacoustophotonics presented in this paper.

REFERENCES

1. A. Mandelis, "Diffusion Waves and their Uses", *Physics Today*, **53**, Part I, 29-34, 2000.
2. R. Hibst, K. Konig, "Device for Detecting Dental Caries", US Pat, 5,306,144, 1994.
3. A. Lussi, S. Imwinkelried, N.B. Pitts, C. Longbottom, and E. Reich, "Performance and Reproducibility of a Laser Fluorescence System for Detection of Occlusal Caries *in vitro*", *Caries Res*, **33**, 261-266, 1999.

4. A. Mandelis, L. Nicolaides, C. Feng, and S.H. Abrams, "Novel Dental Depth Profilometric Imaging Using Simultaneous Frequency-Domain Infrared Photothermal Radiometry and Laser Luminescence", *Biomedical Optoacoustics. Proc SPIE*, A. Oraevsky (ed), **3916**, 130-137, 2000.
5. L. Nicolaides, A. Mandelis, and S.H. Abrams, "Novel Dental Dynamic Depth Profilometric Imaging Using Simultaneous Frequency-Domain Infrared Photothermal Radiometry and Laser Luminescence", *J Biomed Opt*, **5**, 31-39, 2000.
6. A. Mandelis, "Review of progress in theoretical, experimental, and computational investigations in turbid tissue phantoms and human teeth using laser infrared photothermal radiometry, *Thermosense XXIV Proc SPIE*, X.P. Maldague and A.E. Rozlosnik (ed), **4710**, 373-383, 2002.
7. V. G. Andreev, A. A. Karabutov, S. V. Solomatin, E. V. Savateeva, V. Aleynikov, Y. Z. Zhulina, R. D. Fleming, and A. A. Oraevsky, *Biomedical Optoacoustics Proc. SPIE*, A. A. Oraevsky (ed), **3916**, 36-47, 2000.
8. C. G. A. Hoelen, R. G. M. Kolkman, M. Letteboer, R. Berendsen and F. F. de Mul, "Photoacoustic tissue scanning (PATs)", *Optical Tomography and Spectroscopy of Tissue III Proc. SPIE*, **3597**, 336-343, 1999.
9. P. C. Beard and T. N. Mills, "An optical detection system for biomedical photoacoustic imaging", *Biomedical Optoacoustics Proc. SPIE*, A. A. Oraevsky (ed), **3916**, 100-109, 2000.
10. *Biomedical Optoacoustics Proc. SPIE*, A. A. Oraevsky (ed), **3916**, 2000.
11. *Biomedical Optoacoustics II Proc. SPIE*, A. A. Oraevsky (ed), **4256**, 2001.
12. A. J. Welch and M. C. van Gemert, Eds., *Tissue Optical Properties and Laser-Tissue Interactions*, AIP, New York, 1995.
13. A.P. Gibson, J.C. Hebden and S.R. Arridge, "Recent advances in diffuse optical imaging", *Phys. Med. Biol*, **50**, R1-R39, 2005.
14. D. McComb and L.E. Tam, "Diagnosis of Occlusal Caries: Part I. Conventional Methods", *J Can Dent Assoc*, **67**, 454-457, 2001.
15. M. Munidasa and A. Mandelis, *Principles & Perspectives of Photothermal & Photoacoustic Phenomena Vol. 1*, A. Mandelis (ed), Photothermal Imaging and Microscopy: 299-367, Elsevier, New York, 1992.
16. L. Nicolaides, C. Feng, A. Mandelis, and S.H. Abrams, "Quantitative dental measurements by use of simultaneous frequency-domain laser infrared photothermal radiometry and luminescence", *Appl Opt*, **41**, 768-777, 2002.
17. W.S. Brown, W.A. Dewey and H.R. Jacobs, "Thermal Properties of Teeth", *J Dent Res*, **49**, 752-754, 1970.
18. G. Busse and H.G. Walther, *Principles & Perspectives of Photothermal & Photoacoustic Phenomena Vol. 1*, A. Mandelis (ed), Photothermal nondestructive evaluation of materials with thermal waves: 205-298, Elsevier, New York, 1992.
19. R. Heinrich-Weltzien, K.L. Weerheijm, J. Kühnisch, T. Oehme and L. Stösser L, "Clinical evaluation of visual, radiographic, and laser fluorescence methods for detection of occlusal caries", *J Dent Child*, **69**, 127-132, 2002.
20. A. Ishimaru, *Wave Propagation and Scattering in Random Media Vol. 1*, Academic, New York, 1978.
21. T. J. Farrell, M. S. Patterson and B. Wilson, "A diffusion theory model of spatially resolved, steady-state diffuse reflectance for the noninvasive determination of tissue optical properties *in-vivo*", *Med. Phys.*, **19**, 879-888, 1992.
22. W. M. Star and J. P. A. Marijnissen, "New trends in photobiology (invited review) light dosimetry: status and prospects", *J. Photochem. Photobiol.*, **B1**, 149-167, 1987.
23. A. Mandelis, *Diffusion-Wave Fields: Mathematical Methods and Green Functions*, Chap.10: 663 – 708, Springer-Verlag, New York, 2001.
24. A. Karabutov and V. Gusev, *Laser Optoacoustics*, Chap. 2, AIP Press, New York, 1993.
25. Y.Fan, A.Mandelis, G.Spiro and I.A.Vitkin, "Development of a laser photothermoacoustic frequency-swept system for subsurface imaging: Theory and experiment", *J. Acoust. Soc. Am.*, **116**, 3523-3533, 2004.
26. M. I. Skolnik, *Radar Handbook*, Chap.10, McGraw-Hill, NY 1990.
27. R.O.Nielsen, "Sonar signal processing", Artech House, Boston, 1991.
28. R.Huber, K.Taira, M.Wojtkowski, T.H.Ko, J.G.Fujimoto and K.Hsu, "High speed frequency swept light source for Fourier domain OCT at 20 kHz A-scan rate", *Photonics West, Proc. of SPIE*, 2005.
29. G.Hausler and M.W. Lindner, "Coherence radar and spectral radar- new tools for dermatological diagnosis", *J. Biomed. Optics*, **3**, 21-31, 1998.
30. S.Manohar, A.Kharine, J.C.G.van Hespden, W.Steenbergen and T.G.van Leeuwen, "Photoacoustic mammography laboratory prototype: imaging of breast tissue phantoms", *J. Biomed. Opt.*, **9**, 1172-1181, 2004.